



# Structural Basis for the Ribonuclease Activity of a Thermostable CRISPR-Cas13a from *Thermoclostridium caenicola*

Feng Wang <sup>†</sup> Chendi Zhang <sup>†</sup> Haijiang Xu, Wanting Zeng, Lixin Ma and Zhuang Li <sup>\*</sup>

**State Key Laboratory of Biocatalysis and Enzyme Engineering, School of Life Sciences, Hubei University, Wuhan, Hubei 430062, China**

**Correspondence to Zhuang Li:** zhuangli@hubu.edu.cn (Z. Li) @Zhuang\_L (Z. Li)  
<https://doi.org/10.1016/j.jmb.2023.168197>

**Edited by Konstantin Severinov**

## Abstract

The RNA-targeting type VI CRISPR-Cas effector complexes are widely used in biotechnology applications such as gene knockdown, RNA editing, and molecular diagnostics. Compared with Cas13a from mesophilic organisms, a newly discovered Cas13a from thermophilic bacteria *Thermoclostridium caenicola* (TccCas13a) shows low sequence similarity, high thermostability, and lacks pre-crRNA processing activity. The thermostability of TccCas13a has been harnessed to make a sensitive and robust tool for nucleic acid detection. Here we present the structures of TccCas13a-crRNA binary complex at 2.8 Å, and TccCas13a at 3.5 Å. Although TccCas13a shares a similarly bilobed architecture with other mesophilic organism-derived Cas13a proteins, TccCas13a displayed distinct structure features. Specifically, it holds a long crRNA 5'-flank, forming extensive polar contacts with Helical-1 and HEPN2 domains. The detailed analysis of the interaction between crRNA 5'-flank and TccCas13a suggested lack of suitable nucleophile to attack the 2'-OH of crRNA 5'-flank may explain why TccCas13a fails to cleave pre-crRNA. The stem-loop segment of crRNA spacer toggles between double-stranded and single-stranded conformational states, suggesting a potential safeguard mechanism for target recognition. Superimposition of the structures of TccCas13a and TccCas13a-crRNA revealed several conformational changes required for crRNA loading, including dramatic movement of Helical-2 domain. Collectively, these structural insights expand our understanding into type VI CRISPR-Cas effectors, and would facilitate the development of TccCas13a-based applications.

© 2023 Elsevier Ltd. All rights reserved.

## Introduction

CRISPR-Cas systems offer adaptive immunity in bacteria and archaea to fight invasion of mobile genetic elements (MGEs) via RNA-guided cleavage of target nucleic acids.<sup>1–5</sup> CRISPR systems can be generally divided into two classes and six types.<sup>6–8</sup> Class 2 CRISPR-Cas system, including type II, V and VI,<sup>9–13</sup> adopts a single-protein multi-domain nuclease, and has been widely used for genome editing and molecular diagno-

tics.<sup>14,15</sup> RNA-targeting CRISPR-Cas effectors have been developed into various tools for manipulating specific RNA molecules, such as site-specific RNA editing,<sup>16</sup> RNA knockdown<sup>17</sup> and molecular diagnostics.<sup>16</sup>

RNA editing offers a tool for temporary and reversible changes in gene function, avoiding permanent changes to the genome in DNA editing. Besides targeting DNA, Cas9 from type II system<sup>13</sup> and Cas12g from type V system are also capable of targeting RNA.<sup>18,19</sup> In contrast, type VI

Cas13 effectors exclusively target RNA<sup>20</sup> and have been widely used in RNA-related applications. Recently discovered single-subunit type III effectors, including gRAMP<sup>21</sup> and Cas7-11,<sup>22</sup> provided new potential for *in vivo* RNA application.

Type VI CRISPR-Cas systems are characterized by the large multi-domain nuclease with a composite active site consisting of two highly divergent higher eukaryotes and prokaryotes nucleotide-binding (HEPN) domains.<sup>20,23,24</sup> Type VI CRISPR-Cas systems target single-stranded RNA (ssRNA), with six subtypes identified (subtypes VI A-D, X, and Y).<sup>25-27</sup> Compared with type VI A-D effectors which contain more than 1000 amino acids (aa), the recently identified type VI-X and type VI-Y effectors, and miniature Cas13bt contains around 800 aa, facilitating the therapeutic delivery via adeno-associated virus.<sup>26,28</sup> Besides the programmable *cis*-cleavage activity, Cas13a proteins exhibit collateral activity upon activation by target RNA, leading to non-specific degradation of surrounding RNA without apparent sequence specificity.<sup>16</sup> Cas13a has thus been repurposed as nucleic acid detection, such as SHERLOCK technique.<sup>29</sup>

While Cas13a from different species, including *Leptotrichia shahii* (LshCas13a),<sup>30</sup> *Leptotrichia buccalis* (LbuCas13a),<sup>31</sup> *Lachnospiraceae bacterium* (LbaCas13a),<sup>32</sup> *Listeria seeligeri* (LseCas13a),<sup>33</sup> and *Rhodobacter capsulatus* (RcCas13a),<sup>34</sup> have been extensively studied from a biochemical and structural aspect,<sup>27,35</sup> a newly discovered Cas13a from thermophilic bacteria *Thermoclostridium caenicola* (TccCas13a) shows distinct characteristics.<sup>36</sup> TccCas13a was found to contain 1225 aa, and shows low sequence similarity with aforementioned Cas13a proteins. The melting temperature of TccCas13a is around 70 °C, much higher than that of aforementioned Cas13a proteins.<sup>36</sup> It shows robust target cleavage and collateral cleavage activity at a broad temperature range from 37 °C to 70 °C.<sup>36</sup> Interestingly, it lacks pre-crRNA processing activity which is ubiquitous in other mesophilic Cas13a. Similar with other Cas13a proteins,<sup>31</sup> perfect match between the center of spacer and target RNA is required for TccCas13a cleavage, supporting the existence of a central “seed” region.<sup>37</sup> The thermostability of TccCas13a has been harnessed to make a sensitive and robust tool for nucleic acid detection.<sup>36</sup> In contrast to preexisting immunity found in Cas9 and Cas12 orthologs identified from human pathogenic bacteria,<sup>38</sup> the *Thermoclostridium caenicola* isolated from methanogenic sludge<sup>39</sup> is less likely exposed to human immune system, which makes TccCas13a a promising tool for *in vivo* RNA applications. Collectively, these characteristics motivated us to investigate the underlying working mechanism of TccCas13a.

## Results

### Overall structure of TccCas13a-crRNA

We assembled the binary complex of wild-type TccCas13a with a 60-nt crRNA, and determined the structure at an average resolution of 2.8 Å via cryo-EM (Figure S1 and Table 1). The resulting map allows *ab-initio* model building of most of the protein residues with the exception of several segments (1–16, 27–173, 353–359, 625–653, and 703–711), and unambiguous nucleotides assignment with the exception of some of nucleotides (−36, −35, 16, and 17) (Figure S2).

Despite limited sequence identity with Cas13a from other species (Figure S3, 12.13% with LshCas13a, 16.36% with LbuCas13a, 11.78% with LbaCas13a, 17.01% with LseCas13a, 11.62% with RcCas13a, and 15.76% with LwaCas13a), TccCas13a shows similarly bilobed architecture (Figure S4(A)), consisting of an α-helical REC lobe and a NUC lobe, with the repeat region of the crRNA anchored in the REC lobe and the guide region bound within the channel in the NUC lobe (Figure 1). DALI search shows that LbuCas13a is the closest match with an R.M.S.D. of 6.893.

Consistent with other Cas13a, REC lobe contains NTD domain (1–197) and Helical-1 domain (197–360), and NUC lobe contains HEPN1 domain (360–534 and 806–881), Helical-2 domain (534–806), Linker domain (881–1018), and HEPN2 domain (1018–1225). For NTD domain, only the crRNA-interacting part (1 α-helix and 2 β-strands) is observed, different from the intact NTD domain of other Cas13a proteins<sup>31–34,40</sup> (Figure S4(A)). The Helical-1 domain, HEPN1 domain, Helical-2 domain, and Linker domain are composed of 8, 10, 9 and 5 α-helices respectively. The HEPN2 domain is composed of 9 α-helices and 2 β-strands (Figure S2(B)).

### Interaction between crRNA stem-loop and TccCas13a

The crRNA used for cryo-EM study consists of a 36-nt 5'-handle ranging from U(−36) to C(−1), and a 24-nt guide segment ranging from C1 to A24 (Figure 2(A)). The 5'-handle is further divided into 5'-flank (G(−34) to A(−27)), stem-loop (A(−26) to U(−6)), and 3'-flank (G(−5) to C(−1)) (Figure 2(B)). The first two nucleotides, U(−36) and A(−35), are not observed from the cryo-EM density, due to lack of interaction with TccCas13a. The Helical-1 domain interacts with both the stem-loop and 5'-flank, similar with other Cas13a proteins<sup>31–34,40</sup> (Figure S5(A)). Besides constituting the composite active site, the HEPN2 domain and HEPN1 domain also interact with the 5'-flank and 3'-flank respectively. The Linker domain mainly interacts with the

Table 1 Cryo-EM data collection, refinement and validation statistics.

	TccCas13a(8H4U)	TccCas13a-crRNA (8EWG)
<b>Data collection and processing</b>		
Magnification	105,000	105,000
Voltage (kV)	300	300
Electron exposure (e <sup>-</sup> /Å <sup>2</sup> )	54	54
Defocus range (-μm)	1.2–2.2	1.2–2.2
Pixel size (Å)	0.85	0.85
Symmetry imposed	C1	C1
Initial particle images (no.)	2,309,808	4,922,003
Final particle images (no.)	134,153	645,763
Map resolution (Å)	3.59	2.83
FSC threshold	0.143	0.143
Map resolution range (Å)	3.4–5.0	2.6–4.5
<b>Refinement</b>		
Initial model used	PDB:8EWG	None
Model resolution (Å)	3.52	2.97
FSC threshold	0.5	0.5
Model resolution range (Å)	3.3–5.0	2.6–4.5
Map sharpening B factor (Å <sup>2</sup> )	−150	−70
<b>Model composition</b>		
Non-hydrogen atoms	7944	9616
Protein residues	959	1017
Nucleotides	0	56
<b>B factors (Å<sup>2</sup>)</b>		
Protein	68.04	56.36
Nucleotide	NA	81.63
<b>R.m.s. deviations</b>		
Bond lengths (Å)	0.002	0.004
Bond angles (°)	0.593	0.816
<b>Validation</b>		
MolProbity score	1.89	1.90
Clashscore	8.53	5.30
Poor rotamers (%)	1.28	1.43
Ramachandran plot		
Favored (%)	94.94	91.66
Allowed (%)	5.06	8.34
Disallowed (%)	0.00	0.00

spacer segment, and the Helical-2 domain mainly interacts with the 5'-stem of the spacer segment ([Figures 1\(C\)](#) and [2\(A\)](#)).

The stem-loop consists of a 6-bp stem and a 6-nt loop ([Figure 3](#)). The invariant A(−26)-U(−6) pair, which is conserved across all the Cas13a studied to date and considered as a hallmark of Cas13a crRNA,<sup>32</sup> is observed at the end of the stem-loop ([Figures 2\(B,C\)](#) and [4\(C\)](#)). Different from the 5-bp stem of LbuCas13a,<sup>31</sup> the more base pairing within TccCas13a stem-loop may help increase the thermostability of the crRNA. Introduction of mismatches within the stem (U(−6) to A, G(−9) to C, A(−10) to U, G(−11) to C, and G(−12) to C) caused dramatic loss of target RNA cleavage activity ([Figure 2\(E,F\)](#)). The mismatch G(−14) to C caused mild loss of cleavage activity ([Figure 2\(E,F\)](#)). All the crRNA mismatch didn't cause detectable binding loss to TccCas13a ([Figure S6\(A\)](#)). The stem forms extensive polar contacts with neighboring charged residues via phosphate groups. Alanine substitution

of these residues (R199A, R736A, R1036A, K1152A, K1153A) led to differential loss of target RNA cleavage activity without disrupting the binding to crRNA ([Figures 2\(K,L\)](#) and [S6\(C\)](#)). Specifically, R199A and R736A mildly impaired the cleavage activity, R1036A, K1152A, and K1153A lead to a moderate cleavage activity loss. The loop is exposed to the solvent with a limited number of contacts with nearby NTD and Helical-1 domain ([Figure 3](#)). The base stacking inside the loop is capped by W269 ([Figure 3](#)), and alanine substitution of W269 mildly impaired the cleavage activity of TccCas13a without disrupting the binding to crRNA ([Figures 2\(KL\)](#) and [S6\(C\)](#)).

Besides the structure-specific interaction, the crRNA also interacts with TccCas13a in sequence-specific manner via bulge nucleotides that protrude from 3'-stem, namely C(−13), C(−7), and A(−8). Specifically, C(−13) is buried into a pocket formed by K291 and I296, R19 forms polar contact with the base and the sugar of C(−7), and

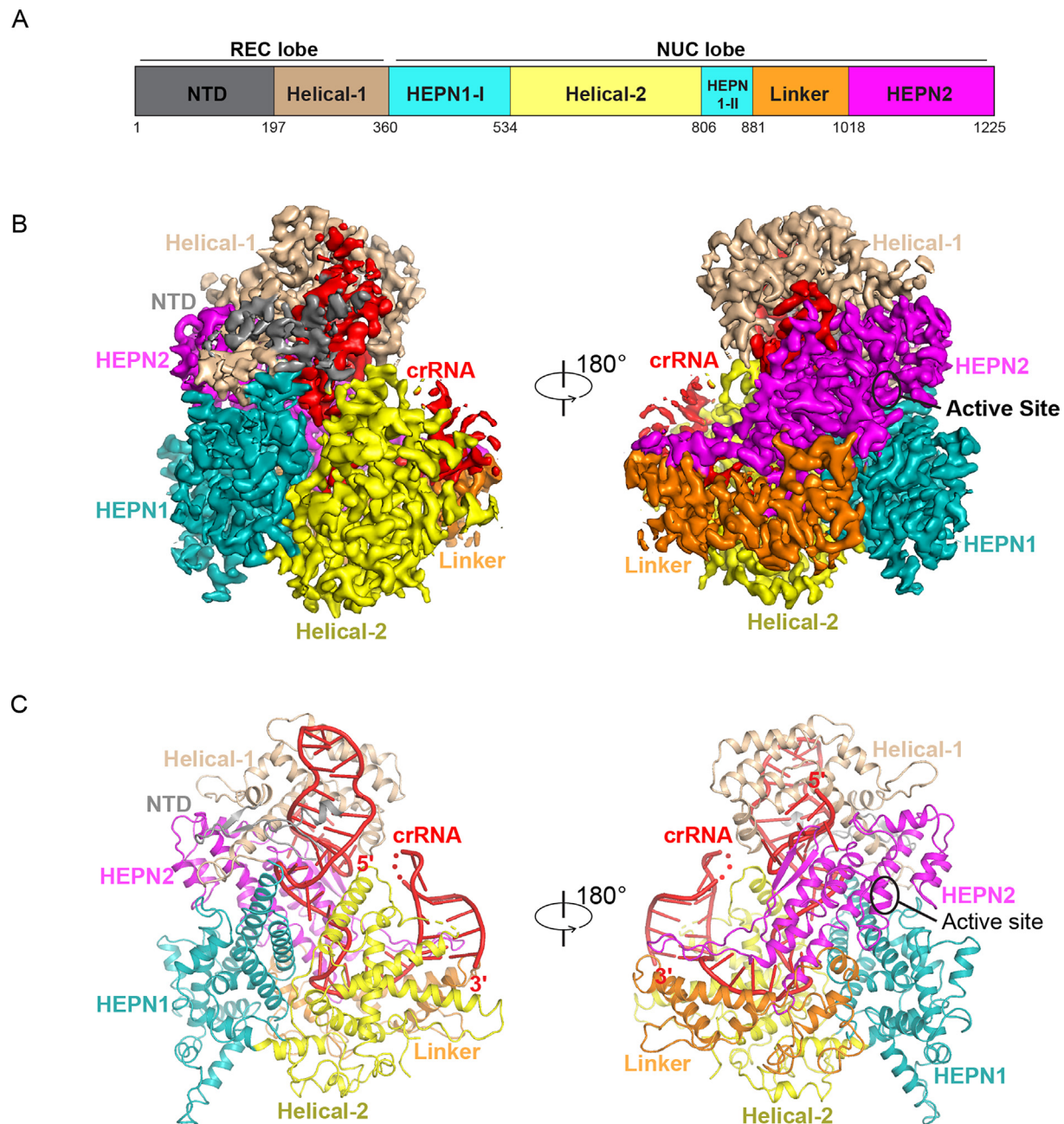


**Figure 1. Overall structure of TccCas13a-crRNA binary complex. (A)** Domain architecture of TccCas13a. **(B)** Cryo-EM density map of TccCas13a-crRNA. TccCas13a is color-coded based on A, and crRNA is colored in red. **(C)** Overall structure of TccCas13a-crRNA complex. The color code is the same as in B.

A(-8) is sandwiched by R842, Q577 and Q735 (Figure 2(D)). Notably, the 2-nt bulge (usually in “AC” motif) is also observed in other Cas13a binary complexes and adjacent to the invariant A-U pairs (Figures 4(C) and S7(A)), highlighting its importance in crRNA positioning in the Cas13a effector complex. Purine-pyrimidine switch within this 2-nt bulge abolished the cleavage activity without disrupting the binding to TccCas13a (Figures 2(E,F) and S6(A)). Alanine substitution of these residues (Q735A, Q577A, K291A, R19A, I296A, R842A) lead to cleavage activity loss

differentially without disrupting the binding (Figures 2(G,H) and S6(B)). Specifically, Q735A, Q577A and R842A substitutions had little effect on cleavage activity. R318A and R19A substitutions disrupted cleavage activity. K291A and I296A substitutions mildly impaired the cleavage activity.

#### Spacer region

Trailing the 3'-flank is the 24-nt spacer. The first three nucleotides, C1, C2, and G3, are observed; while A4, A5, and G6 show blurry cryo-EM density, possibly due to lack of interaction with

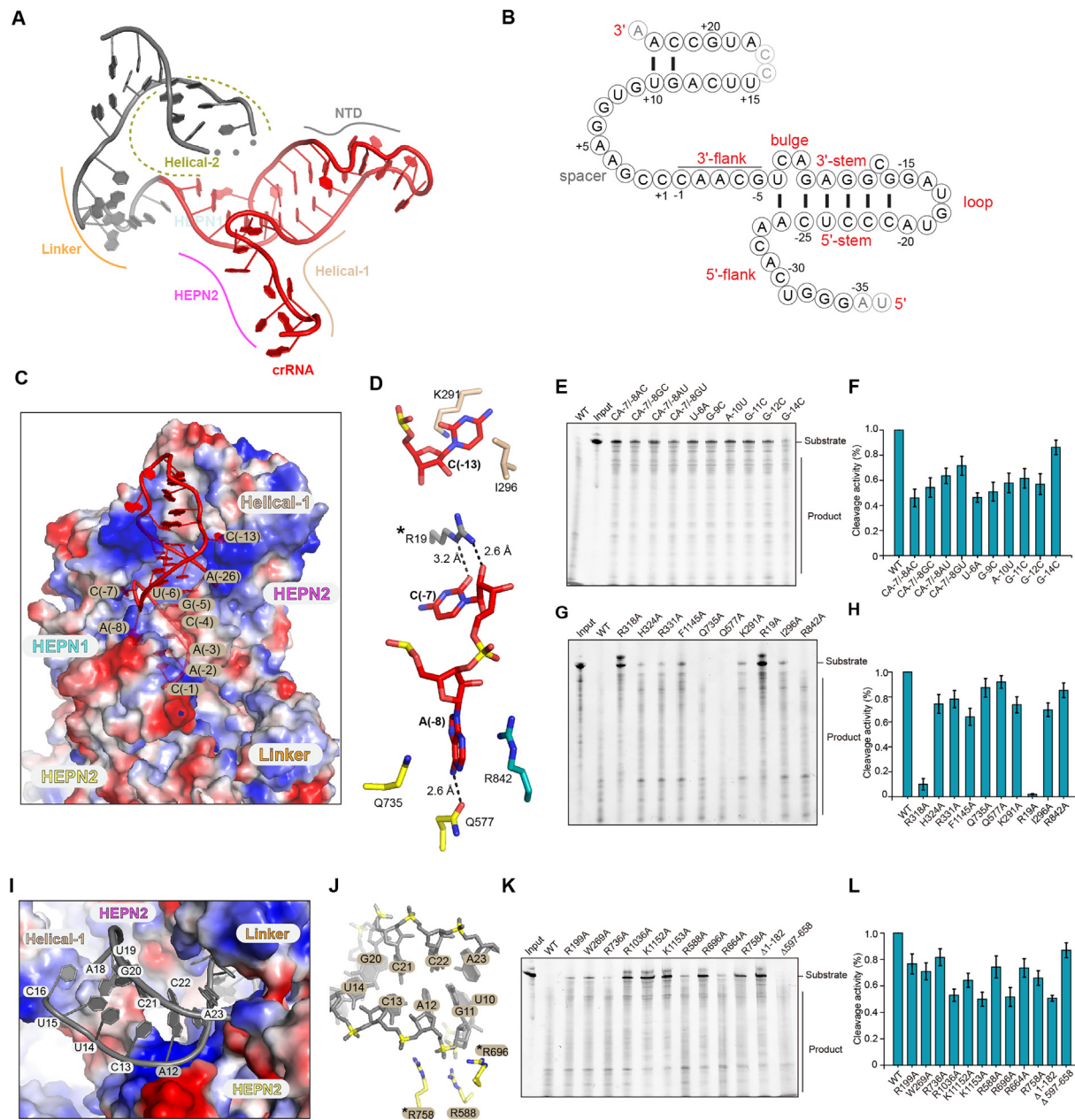


**Figure 2. Interaction between TccCas13a and crRNA.** **(A)** Spatial relationship between crRNA and TccCas13a domains. **(B)** Schematic of crRNA. Invisible nucleotides are colored in gray. **(C)** Electrostatic potential surface representation of TccCas13a and cartoon representation of stem-loop. **(D)** Sequence-specific interaction between bulge residues with TccCas13a. **(E, F)** Target RNA cleavage of TccCas13a using the mutant crRNA, and statistics on the cleavage activity mismatch RNA relative to the WT crRNA. Error bars represent mean  $\pm$  SEM out of  $n = 3$  experiments. **(G, H, K, L)** Target RNA cleavage of TccCas13a using mutant TccCas13a, and statistics on the cleavage activity of mutant TccCas13a relative to the WT TccCas13a. Error bars represent mean  $\pm$  SEM out of  $n = 3$  experiments. **(I)** Electrostatic potential surface representation of TccCas13a and cartoon representation of the stem-loop of spacer. **(J)** Interaction between phosphate groups of 5'-stem and TccCas13a.

surrounding amino acids. G7, U8, and G9 are stabilized by HEPN2 domain, and a sharp turn is introduced between U8 and G9 (Figure 3). The following spacer nucleotides adopt stem-loop configuration, with nucleotides from G11 to U15 constituting the A-form 5'-stem (Figure S7(B),

possible central “seed” due to its A-form conformation), the missing C16 and C17 constituting the loop, and the nucleotides ranging from A18 to A23 constituting the 3'-stem (Figures 2(I) and 3). The base pairing within the stem is only observed between U10 and A23, and

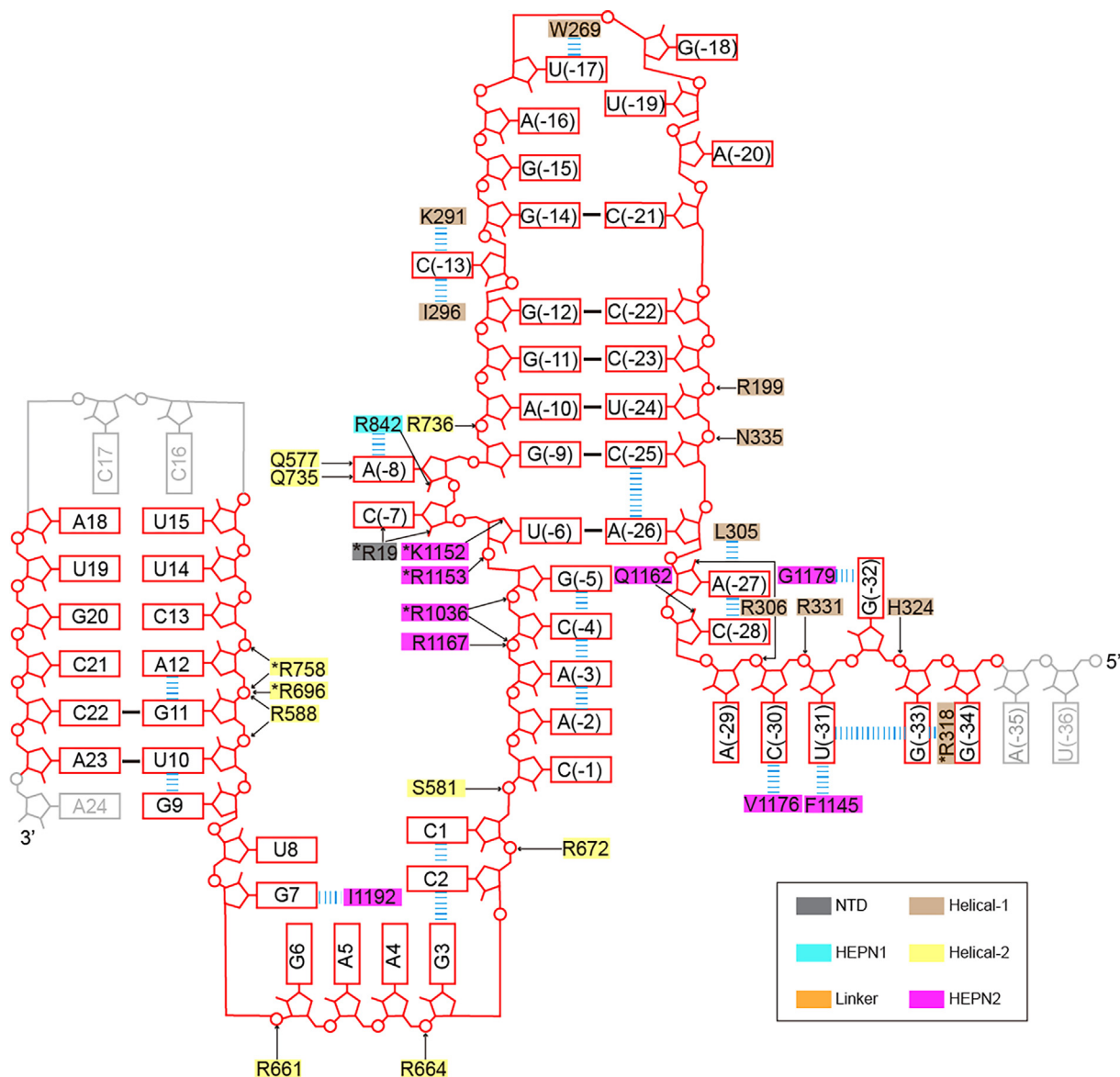


**Figure 3. Schematic of detailed interaction between crRNA and TccCas13a.** The amino acids are color-coded as in Figure 1(A). Polar interactions are shown by black arrows, and the blue dashed lines indicate stacking interactions. Residues critical for cleavage activity are indicated by asterisks.

between G11 and C22 (Figure 2(I)). Such stem-loop configuration within spacer is also observed in the LbuCas13a-crRNA complex.<sup>31</sup> In contrast, LseCas13a and RcCas13a similarly have extended single-stranded configuration which is stabilized by Helical-2 domain<sup>33,34</sup> (Figure S4(B)). As shown in Figure 2(J), R588, R758, and R696 interact with phosphates groups to stabilize the 5'-stem in a sequence non-specific manner; while 3'-stem lacks interaction with TccCas13a amino acids. Alanine substitution of these residues (R588A, R696A, R664A, and R758A) led to cleavage activity loss to a different degree (Figure 2(K,L)). Specifically, R588A and R664A had little effect on cleavage activity. R696A and R758A substitutions caused moderate cleavage activity loss. Interestingly,

detailed analysis of the spacer stem-loop (via three-dimensional classification) revealed two conformational states. 66% of the population adopts double-stranded conformation, and 34% adopts 5'-stem-only conformation (Figure S1(C)), highlighting the flexibility of 3'-stem which can be attributed to lack of interactions with TccCas13a.

#### Interaction between crRNA 5'-flank and TccCas13a

The crRNA 5'-flank is sandwiched by Helical-1 and HEPN2 domain, forming extensive polar contacts. While LbaCas13a contains 5-nt crRNA 5'-flank, LbuCas13a, LseCas13a and RcCas13a contain 4-nt crRNA 5'-flank, and LshCas13a

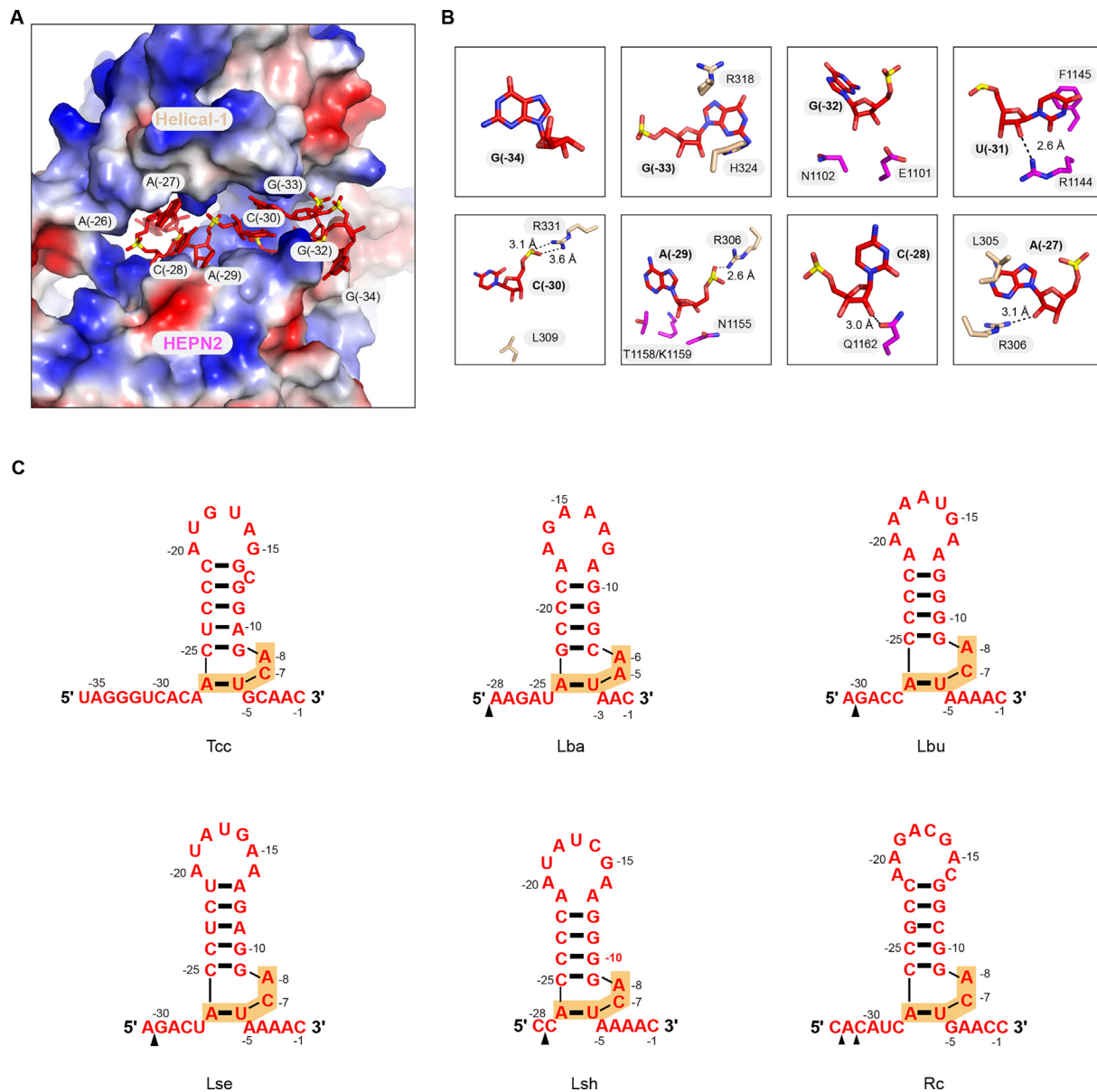


**Figure 4. Interaction between crRNA 5'-flank and TccCas13a.** (A) Electrostatic potential surface representation of TccCas13a and stick representation of crRNA 5'-flank. (B) Detailed interaction between individual nucleotide of crRNA 5'-flank and TccCas13a HEPN2 and Helical-1 domains. (C) Schematic of 5'-handle of Cas13a crRNA from different species. Tcc, *Thermoclostridium caenicola*; Lba, *Lachnospiraceae bacterium*; Lbu, *Leptotrichia buccalis*; Lse, *Listeria seeligeri*; Lsh, *Leptotrichia shahii*; Rc, *Rhodobacter capsulatus*. The triangles indicate cleavage site generated by pre-crRNA processing activity.

contains 1-nt crRNA 5'-flank after pre-crRNA maturation, TccCas13a contains an 8-nt crRNA 5'-flank (Figure 4(A)). The channel to accommodate 5'-flank formed by Helical-1 and HEPN2 domain from different Cas13a proteins are of different length (Figure S5(B)). Amino acids interacting with crRNA 5'-flank include R318, H324, R331, and F1145 (Figure 3). Alanine substitution of these residues (R318A, H324A, R331A, F1145A) lead to cleavage activity loss to a different degree without disrupting the binding (Figures 2(G,H), and S6

(B)). Specifically, H324A, R331A and F1145A substitutions mildly impaired the cleavage activity, while R318A substitution abolished cleavage activity. Notably, the R318 forms cation-π interaction with G(-33), functioning to cap the 5'-flank base stacking. The G(-34) next to R318 becomes more or less flexible, due to lack of amino acid stabilization. G(-33)A and G(-33)C substitution moderately impaired the cleavage activity, highlighting the importance of stacking between R318 and G(-33) (Figure S6(D)).

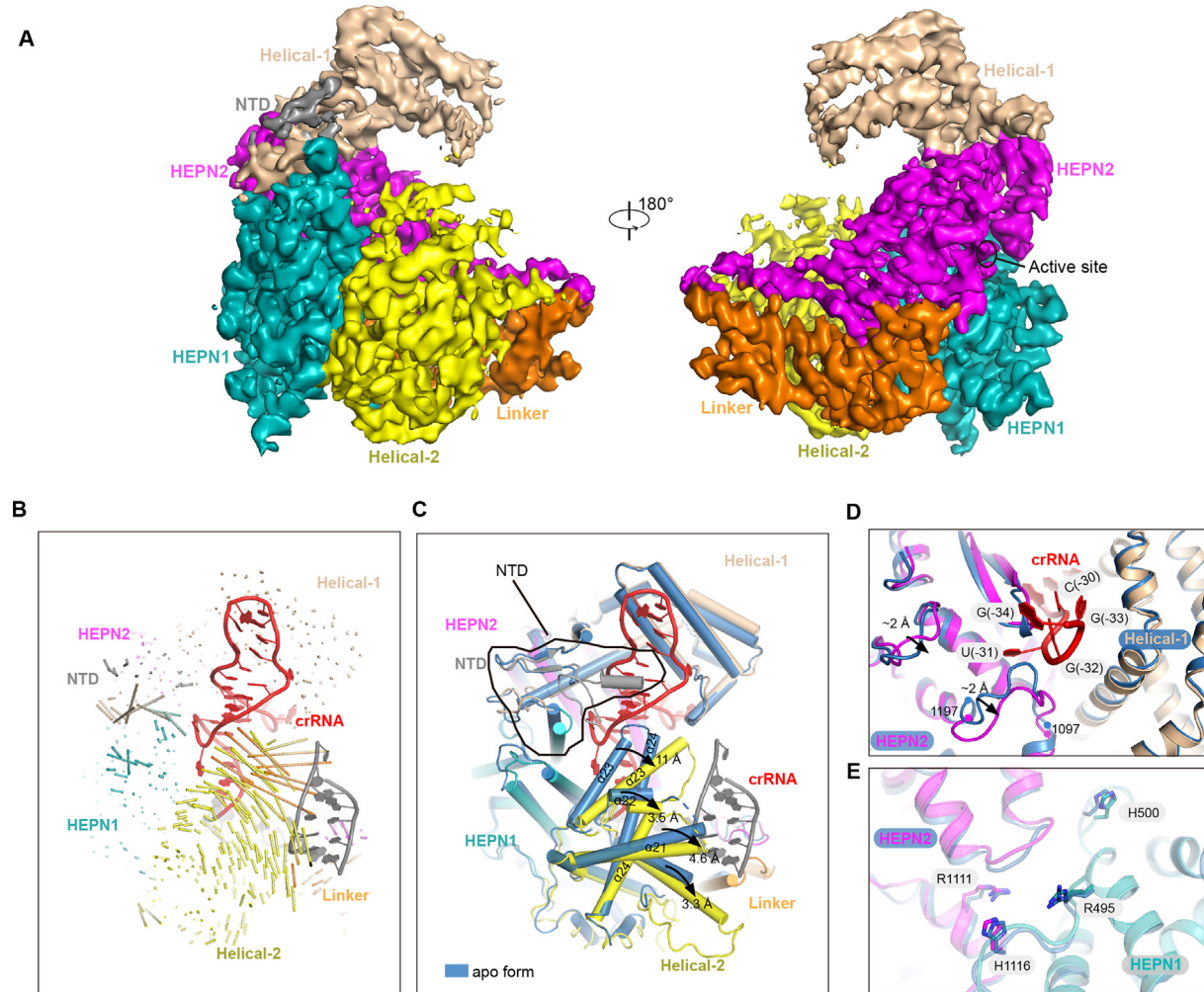


**Figure 5. Conformational change of TccCas13a upon crRNA loading.** (A) Cryo-EM density map of TccCas13a. TccCas13a is color-coded based on Figure 1(A). (B) Schematic representation of TccCas13a domain movement. Vector length corresponds to the translational distance. (C) Cartoon representation of TccCas13a domain movement. The movement direction is indicated by arrows. (D) Conformational change of HEPN2 and Helical-1 domain on the interface of crRNA 5'-flank. (E) Conformational change of composite active sites on HEPN1 and HEPN2 domains. (C-E) TccCas13a-crRNA is color-coded based on Figure 1(A), while TccCas13a is colored blue.

Pre-crRNA processing is a generic and conserved activity which is independent of cleavage activity within Cas13a family.<sup>35,41</sup> Pre-crRNA processing happen at site distal from the cleavage site.<sup>30</sup> Previous biochemical and structural study established a metal ion-independent acid-base mechanism in which the 2'-hydroxyl (2'-OH) nucleophilically attacks the scissile phosphate in the 3' position, and the 2'-OH needs to be deprived of proton to be nucleophilic.<sup>32,35</sup> Intriguingly, Cas13a from a thermophilic bacterium *Herbinix hemicellulosilytica* (HheCas13a) and TccCas13a lack of *in-vitro* pre-crRNA processing activity.<sup>36,41</sup> Structure-based multi-sequence alignment showed that amino acids important for pre-crRNA processing of LbaCas13a are mostly missing in TccCas13a<sup>32</sup> (Figure S3). To further exclude the possibility that TccCas13a pre-crRNA could be

cleaved elsewhere within 5'-flank, a detailed scan of interactions between crRNA 5'-flank (especially 2'-OH) and nearby amino acids, were performed to identify any potential nucleophile to attack the 2'-OH (Figure 4(B)). Specifically, G(-34) has no interacting residues. G(-33) forms cation-π interaction with R318, without protein residues close to 2'-OH. Although in spatial proximity, the sidechains of N1102 and E1101 misalign with the 2'-OH of G(-32). F1145 stacks with nucleobase of U(-31), and the R1144 which is positively charged and cannot be a nucleophile, forms hydrogen bond with 2'-OH. Phosphate group of C(-30) forms charged interaction with R331, and the only residue around the 2'-OH of C(-30) is L309, T1158, K1159, and N1155 misalign with 2'-OH of A(-29). The neutral sidechain of Q1162 forms polar contact with 2'-OH of C(-28). L305 caps the nucleobase stacking of

crRNA 5'-flank, and the R306 forms polar contact with 2'-OH. These observations suggested that lack of suitable nucleophile to attack the 2'-OH of crRNA 5'-flank may explain why TccCas13a lacks pre-crRNA cleavage activity.

### Conformational change of TccCas13a upon crRNA loading

To understand the underlying mechanism for crRNA loading, TccCas13a in apo-form was determined at 3.5 Å resolution (Figure S8). The overall structure is similar to that of TccCas13a-crRNA (Figure 5(A)). Structure comparison between TccCas13a and TccCas13a-crRNA revealed a few conformational changes upon crRNA loading (Figure 5(B)). First, while most part of the NTD domain is missing from both structures, part of NTD domain (17–26 and 174–181) that interacts with the stem-loop gets stabilized upon crRNA loading. Deletion of NTD domain abolished the target RNA cleavage activity (Figure 2(K,L)), highlighting the indispensability of NTD domain. In contrast, other flexible loop (such as 597–658) is not important for the cleavage activity (Figure 2(K,L)). Second, the helix  $\alpha$ 23 of Helical-2 domain rotates outwards by about 11.6 Å to accommodate the stem-loop of crRNA (Figure 5(C)). Similar conformational change was also observed in LshCas13a-crRNA.<sup>30</sup> Meanwhile, a segment from helix  $\alpha$ 24 (748–755) transforms from helix to loop to interact with the seed region of spacer (Figure 5(C)). Other  $\alpha$ -helices, such as  $\alpha$ 18,  $\alpha$ 21 and  $\alpha$ 22, move less dramatically (Figure 5(C)).

Surprisingly, minimal conformational change is observed around crRNA 5'-flank (Figure 5(D)). The most obvious conformational change lies in the loop (1097–1197) that flips outwards to accommodate the nucleobase of U(–31) (Figure 5(D)). This minimal conformational change indicates the channel accommodating crRNA 5'-flank is pre-formed. Other domains, such as HEPN1 and HEPN2, remain largely unchanged. For example, the catalytic residues from HEPN1 and HEPN2 domain (R495, H500, R1111, and H1116), remain far apart and conformationally the same after crRNA loading (Figure 5(E)), indicating that TccCas13a stays inactive in the apo-form, crRNA loading doesn't lead to conformational change of the catalytic center, and TccCas13a only gets activated by target RNA engagement.

## Discussion

In this study, we determined the structures of the thermostable TccCas13a protein with and without its cognate crRNA. The most unique structural feature of TccCas13a-crRNA effector complex is that the crRNA adopts an 8-nt-long crRNA 5'-flank to extensively interact with TccCas13a, which

might help TccCas13a work in high temperature environment. Besides TccCas13a, Cas13a from thermophilic bacterium *Herbinix hemicellulosilytica* is also incapable of cleaving pre-crRNA,<sup>36,41</sup> suggesting the thermostability of these two Cas13a proteins and the lack of pre-crRNA processing activities are somehow related. Besides, Cas13bt3 (also called Cas13X.1) was unable to process the pre-crRNA *in vitro* either.<sup>42</sup> These observations suggest that type VI CRISPR-Cas system may evolve to discard the pre-crRNA processing activity for certain reasons, such as maintaining a compact protein size, or adapting to high living temperature. The absence of pre-crRNA processing activity in the type VI system is perhaps not as rare as we assumed.

Previous reports on TccCas13a support the existence of a central "seed" region, in which mismatch to target RNA is poorly tolerant and leads to dramatic loss of cleavage activity,<sup>31</sup> our structure suggests the structurally ordered A-form 5'-stem of the spacer stem-loop, might serve as the possible central "seed". Furthermore, for the first time we observed a conformational transition of the spacer stem-loop from the double-stranded state to 5'-stem-only state, which suggested a safeguard mechanism that only the perfectly matched target RNA at seed region is capable of displacing the 3'-stem to pair with the 5'-stem, and then initiate the crRNA-target RNA duplex formation. However, single-molecule FRET or other biophysics techniques will be needed to further confirm this conformational transition observed from cryo-EM analysis.

Pre-crRNA processing and target cleavage are two independent activities, and happen at two distal sites.<sup>35</sup> However, RNA cleavage activity by the crRNA-processing inactive mutant was significantly reduced for all spacer sequences in the crRNA array, indicating that while pre-crRNA processing is not necessary for targeting, it enhances activity by liberating crRNAs from the CRISPR array.<sup>41</sup> Therefore, lack of pre-crRNA processing of TccCas13a and HheCas13a raises a fundamental question of whether an alternative mechanism of pre-crRNA processing exists in these systems. Yan *et al* reported a pre-crRNA processing mechanism in which crRNAs of *Neisseria* spp. cells are directly transcribed from promoters that are embedded within each repeat, yielding crRNA 5' ends formed by transcription instead of by processing.<sup>43</sup> However, the direct repeat sequence of TccCas13a and HheCas13a shows little sequence identity to the –35 element and –10 element for bacteria transcription.<sup>44</sup> Genome analysis revealed that, *Thermoclostridium caenicola* encodes about 1084-nt pre-crRNA containing 12 32-nt repeats and 12 ~35-nt spacers, *Herbinix hemicellulosilytica* encodes about 512-nt pre-crRNA containing six 32-nt repeats and six ~35-nt spacers (Figure S9). Simulated structures of crRNA with native spacer

sequence of *Thermoclostridium caenicola* support the formation of spacer stem-loop (Figure S9(B)). Besides type VI CRISPR-Cas system, *Thermoclostridium caenicola* also encodes type I-C and type III-A CRISPR-Cas systems which utilize Cas5c and Csm5 nuclease for pre-crRNA processing respectively<sup>45</sup> (Figure S9(A)). Given the previous report showing that maturation of crRNAs from different CRISPR loci is sometimes catalyzed by the same processing enzyme,<sup>46</sup> it is therefore tempting to hypothesize that TccCas13a might utilize the Cas5c or Csm5 to process the pre-crRNA. However, we didn't find any other CRISPR-Cas system or any well-studied nuclease that is possibly involved in the CRISPR-Cas system from the *Herbinix hemicellulosilytica* genome, which suggested some unknown nucleases might be involved in the pre-crRNA processing. The underlying mechanism of crRNA maturation still needs further investigation.

## Materials and Methods

**Molecular cloning and mutagenesis:** The codon-optimized TccCas13a gene was ligated into pET28a vector by T5 exonuclease-dependent assembly to introduce C-ter His-tag. Single-site mutations were introduced by the QuikChange site-directed mutagenesis method. Large-fragment deletion was introduced by ligating inverse PCR-amplified backbone with DNA oligonucleotides encoding a flexible linker. All plasmids were verified by DNA sanger sequencing.

**Protein expression and purification:** *E. coli* strain BL21(DE3) was transformed with wild-type (WT) or mutant pET28a-TccCas13a plasmids. Single colonies of the resulting transformants were used to inoculate 10 ml LB broth containing 50 µg/ml Kanamycin, and cultures were incubated 16 h at 37 °C with shaking. Aliquots (10 ml) were used to inoculate 1 L LB broth containing 50 µg/ml Kanamycin. After shaking at 37 °C until OD<sub>600</sub> reaches 0.6, the cultures were induced by addition of IPTG to 0.4 mM, and incubated at 18 °C for 16 h. Then, cells were harvested by centrifugation (6000 rpm; 10 min at 4 °C), resuspended in 40 ml buffer A (20 mM Tris-HCl, pH 7.5, 200 mM NaCl, 2 mM DTT) and lysed using a JN-02C cell disrupter (JNBIO, Inc.). The lysate was centrifuged (16000 rpm; 45 min at 4 °C), and the supernatant was loaded onto a 5 ml gravity column of Ni-NTA agarose equilibrated with buffer A. The column was washed with 50 ml buffer A containing 20 mM imidazole and eluted with 10 ml buffer A containing 100 mM imidazole. The samples were further purified by 1-ml HiTrap Heparin HP column (Smart-Lifesciences, Ltd.) equilibrated in buffer A and eluted with a 10 ml linear gradient of 0.2–0.7 M NaCl. Fractions containing wild-type or mutant TccCas13a were pooled and stored at –80 °C.

**TccCas13a-crRNA complex reconstitution:** The TccCas13a-crRNA complex was reconstituted by incubating purified WT TccCas13a and crRNA at the molar ratio of 1:1.2 on ice for 1 h. The resulting complex was purified on a Superdex 200 Increase 10/300 gel filtration column (Cytiva, Inc.) in buffer containing 20 mM Tris-HCl, pH 7.5, 150 mM NaCl, 2 mM DTT.

**In vitro transcription of target RNA and crRNA mutants:** The 60-nt crRNA was synthesized from GenScript Biotech Inc. 400-nt target RNA and 60-nt crRNA mutants were transcribed with T7 *in vitro* transcription Kit (K0441, ThermoFisher). DNA template for RNA transcription was generated via DNA oligo annealing. Transcription reactions were performed at 37 °C for 4 h with a volume of 20 µL containing 4 µL transcription buffer, 2 µL NTP each, 2 µL T7 RNA polymerase, and 2 µg annealed double strand DNA. After transcription, reaction mixture was digested at 37 °C for 15 min with 4 µL DNase I. 115 µL DEPC H<sub>2</sub>O was added to reach a final volume of 150 µL. Digestion was terminated by addition of 150 µL phenol and 150 µL chloroform. After vortex and centrifugation, RNA in the supernatant was transferred to a new tube and precipitated by adding 15 µL 3 M sodium acetate solution and 400 µL ethanol, then incubated at –20 °C for 30 min and centrifugated, the RNA pellet was resuspended in DEPC H<sub>2</sub>O and stored at –80 °C.

**In vitro cleavage assays:** *In vitro* cleavage assays were based on the protocol described in Ahmed Mahas *et al.*,<sup>36</sup> with minor modification. WT and mutants TccCas13a cleavage reactions were performed at 37 °C with target RNA, crRNA or crRNA mutants. Briefly, cleavage reactions were carried out in 10 µL reaction volume with 250 nM of either WT or mutant Cas13a proteins, 250 nM of either crRNA or crRNA mutants, and 500 nM of target RNA in reaction buffer (20 mM Tris-HCl pH 8.8, 50 mM KCl, 10 mM (NH<sub>4</sub>)<sub>2</sub>SO<sub>4</sub>, 6 mM MgSO<sub>4</sub>, 0.1% Tween 20); the reactions were then incubated at 37 °C for 5 min. The samples were then boiled at 70 °C for 3 min in 2X RNA loading dye, and cooled down on ice for 3 min before loading into an 8% Urea-PAGE gel. Electrophoresis was conducted at 120 V for 90 min. After stained with SYBR Gold dye (S11494, ThermoFisher) for 5 min and briefly washed with 1X TBE buffer, the gels were visualized by a Bio-Rad Imaging system. All experiments were performed in three independent replicates.

**Electrophoretic Mobility Shift Assay:** Electrophoretic Mobility Shift Assay (EMSA) was performed in the reaction buffer containing 20 mM Tris pH 8.0, 200 mM NaCl, 2 mM β-ME and 2% glycerol. The purified WT or mutant TccCas13a proteins (80 µg) were incubated with crRNA or crRNA mutants or non-cognate RNAs (1: GUACUACAUUGCUAUCCGAGUAACUGCCGA AGGUGUGACUUCCAUGCCAA. 2: GCAUGUAC GGCU CCAAGGCCUACGUGAAGCACUCGACC

UUUUUAGGUCG) at a ratio of 1:1.2 on ice for 30 min. 1/40 of the samples were loaded onto a 1.5% TAE agarose gel and run 40 min at 90 V at 4 °C. The gels were visualized by staining with ethidium bromide. All experiments were performed in three independent replicates.

**Electron microscopy:** Aliquots of 4 µL samples (0.8 mg/ml for TccCas13a-crRNA sample and 0.7 mg/ml for TccCas13a sample) were applied to glow-discharged Quantifoil holey carbon girds (Cu, R1.2/1.3, 300 mesh). The grids were blotted with force 2 for 3 s and plunged into liquid ethane using a Vitrobot. Cryo-EM data were collected with a Titan Krios microscope (FEI) operated at 300 kV and images were collected using EPU<sup>47</sup> at a nominal magnification of 105,000x (resulting in a calibrated physical pixel size of 0.85 Å/pixel) with a defocus range from -1.2 µm to -2.2 µm. The images were recorded on a K3 summit electron direct detector in super-resolution mode at the end of a GIF-Quantum energy filter operated with a slit width of 20 eV. A dose rate of 15 electrons per pixel per second and an exposure time of 2.5 s were used, generating 40 movie frames with a total dose of ~54 electrons per Å<sup>2</sup>. A total of 1954 and 4367 movie stacks were collected for TccCas13a and TccCas13a-crRNA respectively (Table 1).

**Image processing:** The movie frames were imported to RELION-3.<sup>48</sup> Movie frames were aligned using MotionCor2<sup>49</sup> with a binning factor of 2. Contrast transfer function (CTF) parameters were estimated using Gctf.<sup>50</sup> Around 9000 particles were auto-picked without template to generate 2D averages for subsequent template-based auto-picking.

For TccCas13a-crRNA dataset, 4,922,003 particles were auto-picked and extracted from the dose weighted micrographs. 2D classification was performed to exclude false and bad particles that fall into 2D averages with poor features. 2,421,671 particles were selected for further processing. Particles from different views were used to generate initial model in cryoSPARC.<sup>51</sup> 3D classification was performed to distinguish different conformational states. 645,763 particles were used for final 3D refinement, CTF refinement, and Bayesian polishing, converging at 2.8 Å resolution. Details of the cryo-EM image processing is summarized in Table 1.

For TccCas13a dataset, 2,309,808 particles were auto-picked and extracted from the dose weighted micrographs. 2D classification was performed to exclude false and bad particles that fall into 2D averages with poor features. 561,050 particles were selected for further processing. Particles from different views were used to generate initial model in cryoSPARC. 3D classification was performed to distinguish different conformational states. 134,153 particles were used for final 3D refinement, converging at 3.5 Å resolution. Details

of the cryo-EM image processing is summarized in Table 1.

#### Model Building, refinement and visualization:

For model building of TccCas13a-crRNA, predicted structure of TccCas13a from AlphaFold<sup>52</sup> was used for a starter for de novo model building in COOT,<sup>53</sup> and crRNA was *de novo* built. For model building of TccCas13a, TccCas13a from TccCas13a-crRNA was used as starter and manually adjusted in COOT. Model refinement was performed using phenix.real\_space\_refine tool in Phenix.<sup>54</sup> The refinement statistics are summarized in Table 1. Figures were generated via PyMOL and UCSF Chimera.<sup>55</sup>

#### CRediT authorship contribution statement

**Feng Wang:** Methodology, Formal analysis, Investigation, Project administration, Writing – original draft, Data curation. **Chendi Zhang:** Data curation, Formal analysis, Visualization. **Haijiang Xu:** . **Wanting Zeng:** . **Lixin Ma:** Resources.

**Zhuang Li:** Conceptualization, Writing – original draft, Writing – review & editing, Visualization, Supervision, Project administration, Funding acquisition.

#### DATA AVAILABILITY

Cryo-EM reconstruction of TccCas13a and TccCas13a-crRNA have been deposited in the Electron Microscopy Data Bank under the accession numbers EMD-34484 and EMD-28645 respectively. Coordinates for atomic models of TccCas13a and TccCas13a-crRNA have been deposited in the Protein Data Bank under the accession numbers 8H4U and 8EWG respectively.

#### DECLARATION OF COMPETING INTEREST

The authors declare that they have no known competing financial interests or personal relationships that could have appeared to influence the work reported in this paper.

#### Acknowledgement

We thank the staff members from Cryo-Electron Microscopy Facility of Hubei University for help on data collection and computation. We thank the reviewers for the thoughtful comments and detailed suggestions on the paper.

This work was supported by the National Natural Science Foundation of China (32201004), the Ministry of Science and Technology (2022YFA0911800), the Hubei Provincial Natural Science Foundation (ZRMS2022000096), and

the Scientific Research Program of Hubei Provincial Department of Education.

## Appendix A. Supplementary data

Supplementary data to this article can be found online at <https://doi.org/10.1016/j.jmb.2023.168197>.

Received 30 December 2022;  
Accepted 6 July 2023;  
Available online 11 July 2023

**Keywords:**  
CRISPR-Cas13a;  
structure;  
molecular diagnosis;  
thermostability

† These authors contributed equally to this work.

### Abbreviations:

CRISPR, Clustered regularly interspaced short palindromic repeats; TccCas13a, *Thermoclostridium caenicola* Cas13a; crRNA, CRISPR RNA; MGEs, Mobile genetic elements; HEPN, Higher eukaryotes and prokaryotes nucleotide-binding; ssRNA, single-stranded RNA; LshCas13a, *Leptotrichia shahii* Cas13a; LbuCas13a, *Leptotrichia buccalis* Cas13a; LbaCas13a, *Lachnospiraceae bacterium* Cas13a; LseCas13a, *Listeria seeligeri* Cas13a; RcCas13a, *Rhodobacter capsulatus* Cas13a; NUC, Nuclease lobe; NTD, N-terminal domain; WT, wild-type

## References

- Mohanraju, P. et al, (2016). Diverse evolutionary roots and mechanistic variations of the CRISPR-Cas systems. *Science* **353**, <https://doi.org/10.1126/science.aad5147>.
- Wiedenheft, B., Sternberg, S.H., Doudna, J.A., (2012). RNA-guided genetic silencing systems in bacteria and archaea. *Nature* **482**, 331–338. <https://doi.org/10.1038/nature10886>.
- Marraffini, L.A., (2015). CRISPR-Cas immunity in prokaryotes. *Nature* **526**, 55–61. <https://doi.org/10.1038/nature15386>.
- Jiang, F., Doudna, J.A., (2017). CRISPR-Cas9 Structures and Mechanisms. *Annu. Rev. Biophys.* **46**, 505–529. <https://doi.org/10.1146/annurev-biophys-062215-010822>.
- Hille, F. et al, (2018). The Biology of CRISPR-Cas: Backward and Forward. *Cell* **172**, 1239–1259. <https://doi.org/10.1016/j.cell.2017.11.032>.
- Makarova, K.S. et al, (2015). An updated evolutionary classification of CRISPR-Cas systems. *Nature Rev. Microbiol.* **13**, 722–736. <https://doi.org/10.1038/nrmicro3569>.
- Shmakov, S. et al, (2017). Diversity and evolution of class 2 CRISPR-Cas systems. *Nature Rev. Microbiol.* **15**, 169–182. <https://doi.org/10.1038/nrmicro.2016.184>.
- Koonin, E.V., Makarova, K.S., Zhang, F., (2017). Diversity, classification and evolution of CRISPR-Cas systems. *Curr. Opin. Microbiol.* **37**, 67–78. <https://doi.org/10.1016/j.mib.2017.05.008>.
- Terns, M.P., (2018). CRISPR-based technologies: impact of RNA-targeting systems. *Mol. Cell* **72**, 404–412. <https://doi.org/10.1016/j.molcel.2018.09.018>.
- Dugar, G. et al, (2018). CRISPR RNA-Dependent binding and cleavage of endogenous RNAs by the campylobacter jejuni Cas9. *Mol. Cell* **69**, 893–905.e897. <https://doi.org/10.1016/j.molcel.2018.01.032>.
- Strutt, S.C., Torrez, R.M., Kaya, E., Negrete, O.A., Doudna, J.A., (2018). RNA-dependent RNA targeting by CRISPR-Cas9. *eLife* **7** <https://doi.org/10.7554/eLife.32724>.
- Rousseau, B.A., Hou, Z., Gramelspacher, M.J., Zhang, Y., (2018). Programmable RNA cleavage and recognition by a natural CRISPR-Cas9 system from neisseria meningitidis. *Mol. Cell* **69**, 906–914.e904. <https://doi.org/10.1016/j.molcel.2018.01.025>.
- O'Connell, M.R. et al, (2014). Programmable RNA recognition and cleavage by CRISPR/Cas9. *Nature* **516**, 263–266. <https://doi.org/10.1038/nature13769>.
- Barrangou, R., Doudna, J.A., (2016). Applications of CRISPR technologies in research and beyond. *Nature Biotechnol.* **34**, 933–941. <https://doi.org/10.1038/nbt.3659>.
- Komor, A.C., Badran, A.H., Liu, D.R., (2017). CRISPR-based technologies for the manipulation of eukaryotic genomes. *Cell* **169**, 559. <https://doi.org/10.1016/j.cell.2017.04.005>.
- Cox, D.B.T. et al, (2017). RNA editing with CRISPR-Cas13. *Science* **358**, 1019–1027. <https://doi.org/10.1126/science.aaq180>.
- Abudayyeh, O.O. et al, (2017). RNA targeting with CRISPR-Cas13. *Nature* **550**, 280–284. <https://doi.org/10.1038/nature24049>.
- Yan, W.X. et al, (2019). Functionally diverse type V CRISPR-Cas systems. *Science* **363**, 88–91. <https://doi.org/10.1126/science.aav7271>.
- Li, Z., Zhang, H., Xiao, R., Han, R., Chang, L., (2021). Cryo-EM structure of the RNA-guided ribonuclease Cas12g. *Nature Chem. Biol.* **17**, 387–393. <https://doi.org/10.1038/s41589-020-00721-2>.
- Abudayyeh, O.O. et al, (2016). C2c2 is a single-component programmable RNA-guided RNA-targeting CRISPR effector. *Science* **353**, <https://doi.org/10.1126/science.aaf5573>.
- Hu, C. et al, (2022). Craspase is a CRISPR RNA-guided, RNA-activated protease. *Science* **377**, 1278–1285. <https://doi.org/10.1126/science.add5064>.
- Ozcan, A. et al, (2021). Programmable RNA targeting with the single-protein CRISPR effector Cas7-11. *Nature* **597**, 720–725. <https://doi.org/10.1038/s41586-021-03886-5>.
- Yan, W.X. et al, (2018). Cas13d is a compact RNA-targeting type VI CRISPR effector positively modulated by a WYL-domain-containing accessory protein. *Mol. Cell* **70**, 327–339.e325. <https://doi.org/10.1016/j.molcel.2018.02.028>.
- Smargon, A.A. et al, (2017). Cas13b is a type VI-B CRISPR-associated RNA-guided RNase differentially regulated by accessory proteins Csx27 and Csx28. *Mol. Cell* **65**, 618–630.e617. <https://doi.org/10.1016/j.molcel.2016.12.023>.
- Makarova, K.S. et al, (2020). Evolutionary classification of CRISPR-Cas systems: a burst of class 2 and derived variants. *Nature Rev. Microbiol.* **18**, 67–83. <https://doi.org/10.1038/s41579-019-0299-x>.

26. Xu, C. et al, (2021). Programmable RNA editing with compact CRISPR-Cas13 systems from uncultivated microbes. *Nature Methods* **18**, 499–506. <https://doi.org/10.1038/s41592-021-01124-4>.
27. O'Connell, M.R., (2019). Molecular mechanisms of RNA targeting by Cas13-containing Type VI CRISPR-Cas systems. *J. Mol. Biol.* **431**, 66–87. <https://doi.org/10.1016/j.jmb.2018.06.029>.
28. Kannan, S. et al, (2022). Compact RNA editors with small Cas13 proteins. *Nature Biotechnol.* **40**, 194–197. <https://doi.org/10.1038/s41587-021-01030-2>.
29. Kellner, M.J., Koob, J.G., Gootenberg, J.S., Abudayyeh, O. O., Zhang, F., (2019). SHERLOCK: nucleic acid detection with CRISPR nucleases. *Nature Protoc.* **14**, 2986–3012. <https://doi.org/10.1038/s41596-019-0210-2>.
30. Liu, L. et al, (2017). Two Distant catalytic sites are responsible for C2c2 RNase activities. *Cell* **168**, 121–134. e112. <https://doi.org/10.1016/j.cell.2016.12.031>.
31. Liu, L. et al, (2017). The molecular architecture for RNA-guided RNA cleavage by Cas13a. *Cell* **170**, 714–726.e710. <https://doi.org/10.1016/j.cell.2017.06.050>.
32. Knott, G.J. et al, (2017). Guide-bound structures of an RNA-targeting A-cleaving CRISPR-Cas13a enzyme. *Nature Struct. Mol. Biol.* **24**, 825–833. <https://doi.org/10.1038/nsmb.3466>.
33. Meeske, A.J. et al, (2020). A phage-encoded anti-CRISPR enables complete evasion of type VI-A CRISPR-Cas immunity. *Science* **369**, 54–59. <https://doi.org/10.1126/science.abb6151>.
34. Kick, L.M., von Wrisberg, M.K., Runtsch, L.S., Schneider, S., (2022). Structure and mechanism of the RNA dependent RNase Cas13a from Rhodobacter capsulatus. *Commun Biol* **5**, 71. <https://doi.org/10.1038/s42003-022-03025-4>.
35. East-Seletsky, A. et al, (2016). Two distinct RNase activities of CRISPR-C2c2 enable guide-RNA processing and RNA detection. *Nature* **538**, 270–273. <https://doi.org/10.1038/nature19802>.
36. Mahas, A. et al, (2022). Characterization of a thermostable Cas13 enzyme for one-pot detection of SARS-CoV-2. *Proc Natl Acad Sci U S A* **119**, <https://doi.org/10.1073/pnas.2118260119> e2118260119.
37. Tambe, A., East-Seletsky, A., Knott, G.J., Doudna, J.A., O'Connell, M.R., (2018). RNA Binding and HEPN-Nuclease Activation Are Decoupled in CRISPR-Cas13a. *Cell Rep.* **24**, 1025–1036. <https://doi.org/10.1016/j.celrep.2018.06.105>.
38. Mehta, A., Merkel, O.M., (2020). Immunogenicity of Cas9 Protein. *J. Pharm. Sci.* **109**, 62–67. <https://doi.org/10.1016/j.xphs.2019.10.003>.
39. Shiratori, H. et al, (2009). Clostridium clariflavum sp. nov. and Clostridium caenicola sp. nov., moderately thermophilic, cellulose/cellobiose-digesting bacteria isolated from methanogenic sludge. *Int. J. Syst. Evol. Microbiol.* **59**, 1764–1770. <https://doi.org/10.1099/ijsm.0.003483-0>.
40. Liu, L. et al, (2017). C2c1-sgRNA complex structure reveals RNA-guided DNA cleavage mechanism. *Mol. Cell* **65**, 310–322. <https://doi.org/10.1016/j.molcel.2016.11.040>.
41. East-Seletsky, A., O'Connell, M.R., Burstein, D., Knott, G. J., Doudna, J.A., (2017). RNA Targeting by Functionally Orthogonal Type VI-A CRISPR-Cas Enzymes. *Mol Cell* **66**, 373–383.e373. <https://doi.org/10.1016/j.molcel.2017.04.008>.
42. Nakagawa, R. et al, (2022). Structure and engineering of the minimal type VI CRISPR-Cas13bt3. *Mol Cell* **82**, 3178–3192.e3175. <https://doi.org/10.1016/j.molcel.2022.08.001>.
43. Zhang, Y. et al, (2013). Processing-independent CRISPR RNAs limit natural transformation in *Neisseria meningitidis*. *Mol. Cell* **50**, 488–503. <https://doi.org/10.1016/j.molcel.2013.05.001>.
44. Hook-Barnard, I.G., Hinton, D.M., (2007). Transcription initiation by mix and match elements: flexibility for polymerase binding to bacterial promoters. *Gene Regul Syst Bio* **1**, 275–293.
45. Charpentier, E., Richter, H., van der Oost, J., White, M.F., (2015). Biogenesis pathways of RNA guides in archaeal and bacterial CRISPR-Cas adaptive immunity. *FEMS Microbiol. Rev.* **39**, 428–441. <https://doi.org/10.1093/femsre/fuv023>.
46. Nickel, L. et al, (2013). Two CRISPR-Cas systems in *Methanosarcina mazei* strain Go1 display common processing features despite belonging to different types I and III. *RNA Biol.* **10**, 779–791. <https://doi.org/10.4161/rna.23928>.
47. Thompson, R.F., Iadanza, M.G., Hesketh, E.L., Rawson, S., Ranson, N.A., (2019). Collection, pre-processing and on-the-fly analysis of data for high-resolution, single-particle cryo-electron microscopy. *Nature Protoc.* **14**, 100–118. <https://doi.org/10.1038/s41596-018-0084-8>.
48. Zivanov, J. et al, (2018). New tools for automated high-resolution cryo-EM structure determination in RELION-3. *Elife* **7** <https://doi.org/10.7554/elife.42166>.
49. Zheng, S.Q. et al, (2017). MotionCor2: anisotropic correction of beam-induced motion for improved cryo-electron microscopy. *Nature Methods* **14**, 331–332. <https://doi.org/10.1038/nmeth.4193>.
50. Zhang, K., (2016). Gctf: Real-time CTF determination and correction. *J. Struct. Biol.* **193**, 1–12. <https://doi.org/10.1016/j.jsb.2015.11.003>.
51. Punjani, A., Rubinstein, J.L., Fleet, D.J., Brubaker, M.A., (2017). cryoSPARC: algorithms for rapid unsupervised cryo-EM structure determination. *Nature Methods* **14**, 290–296. <https://doi.org/10.1038/nmeth.4169>.
52. Jumper, J. et al, (2021). Highly accurate protein structure prediction with AlphaFold. *Nature* **596**, 583–589. <https://doi.org/10.1038/s41586-021-03819-2>.
53. Emsley, P., Lohkamp, B., Scott, W.G., Cowtan, K., (2010). Features and development of Coot. *Acta Crystallogr. D Biol. Crystallogr.* **66**, 486–501. <https://doi.org/10.1107/S0907444910007493>.
54. Afonine, P.V. et al, (2018). Real-space refinement in PHENIX for cryo-EM and crystallography. *Acta Crystallogr D Struct Biol* **74**, 531–544. <https://doi.org/10.1107/S2059798318006551>.
55. Pettersen, E.F. et al, (2004). UCSF Chimera—a visualization system for exploratory research and analysis. *J. Comput. Chem.* **25**, 1605–1612. <https://doi.org/10.1002/jcc.20084>.